Available online at www.sciencedirect.com
SCIENCE DIRECT®
Journal of Sound and Vibration 270 (2004) 933–950
JOURNAL OF SOUND AND VIBRATION
www.elsevier.com/locate/jsvi

Frequency-domain prediction of turbofan noise radiation

Y. Özyörük[a,*], E. Alpman[a,1], V. Ahuja[b], L.N. Long[c]

[a] *Department of Aerospace Engineering, Middle East Technical University, 06531 Ankara, Turkey*
[b] *Combustion Research and Flow Technology, Inc., Dublin, PA 18917, USA*
[c] *Department of Aerospace Engineering, Pennsylvania State University, University Park, PA 16802, USA*

Received 1 May 2002; accepted 6 February 2003

Abstract

This paper describes a frequency-domain numerical method for predicting noise radiation from ducted fans, including acoustic treatment and non-uniform background flow effects. The method solves the Euler equations linearized about a mean flow in the frequency domain. A pseudo-time derivative term is added to the frequency-domain equations so that a time marching technique can be employed to drive the acoustic field to steady state explicitly. This approach makes distributed parallel computing more viable for equations of this type and will allow for future use of well-known convergence acceleration techniques, such as multigrid, to obtain the solutions efficiently. Simulations of the JT15D static test inlet are performed including the effects of liners, and the results are compared with experimental data. A generic engine geometry is used for demonstrating further the prediction capability of the code, calculating the attenuation effects of different liner impedances and liner installation locations on the radiated sound fields.

1. Introduction

In an ambitious effort to reduce noise levels in modern turbofan engines, considerable research has been done towards the development of advanced liner technologies. Traditional liners used to attenuate noise in turbofan engines generally consisted of arrays of Helmholtz resonators constructed by bonding fine wire mesh screens to honeycomb-like cavity backed perforates. Not surprisingly, most of the liners constructed in this manner were tuned to resonate with a single dominant frequency. Under NASA's Advanced Subsonic Technology (AST) noise-reduction program several advanced turbofan duct liner concepts have been developed. These include

*Corresponding author. Tel.: +90-312-210-4275; fax: +90-312-210-1272.
E-mail address: yusuf@ae.metu.edu.tr (Y. Özyörük).
[1] Presently at the Department of Aerospace Engineering, Penn State University.

0022-460X/$ - see front matter © 2003 Elsevier Ltd. All rights reserved.
doi:10.1016/S0022-460X(03)00640-0

passive acoustic liners with increased degrees of freedom such as double layers, triple layers and parallel element liners [1]. However, a study on liner performance revealed that passive liners with increased degrees of freedom such as triple layer perforates showed only 2–3 per cent improvement for inlets and between 6 and 10 per cent improvement for fan ducts over 1992 technology. Better liner designs can be facilitated through a better understanding of the fundamental mechanics of non-linear physical phenomena such as fluid acoustic coupling that are associated with liner resonant cavities. Furthermore, issues related to performance of liner materials at grazing flow incidence and varying flow conditions need to be addressed and understood in order both to predict the radiated fan noise accurately and design more effective liner technology. For this to be facilitated, liner performance needs to be analyzed in conjunction with fan noise for engine inlet and exhaust configurations. Until recently, liner analysis was based on empirical models and experimental observations while sound propagation from engine nacelles and exhausts was looked at with radiation and duct propagation codes using hard-wall assumptions. In this paper, we bring about a synthesis of the two problems of liner analysis and sound radiation from engine inlets.

Most of the computational analysis performed in the area of high bypass ratio engine acoustics fall into two broad categories: Direct time-domain approaches [2–7] have become popular and most of the methods in this group are a result of the maturation of computational fluid dynamic (CFD) algorithms that can be applied to aeroacoustic problems. The main advantage of time-domain methods is the ability to handle multifrequency sources in one single simulation. Non-linear effects are also accounted for in time-domain methods through the solution of the full Euler or Navier–Stokes equations. The authors Özyörük and Long [2] developed a parallel, 3-D Euler solver to predict forward-radiated noise of ducted fans. This was later followed by an effort to predict the integrated forward- and aft-radiated noise from turbofan engines [7]. However, the main drawback of time-domain methods relates to treatment of frequency-dependent lining materials. In the past, such treatment of acoustic soft walls with frequency-dependent impedance values has been limited to frequency-domain methods. However, the authors [8] devised and successfully used a z-transform-based formulation for a frequency-dependent impedance condition in time-domain calculations. The continuing work of the present authors with time-domain methods has become quite mature including many realistic effects.

At the other end of the spectrum are frequency-domain methods that represent a second class of noise prediction methods for aircraft engines. Eversman and his co-workers developed a finite-element (FE) code based on the Galerkin method [9,10]. Later, they included acoustic treatment effects in their numerical model [11] and extended it to calculate both fore and aft radiation [12]. Hence, this code became widely used (e.g., Ref. [13]). Eversman's code is based on the solution of the velocity potential equation in the frequency domain including non-uniform background flow effects. This code used the wave envelope technique to find farfield sound in its early developments [10]. Roy and Eversman [14] later incorporated a Kirchhoff integration technique into the FE code, and they showed that accurate farfield predictions can also be obtained efficiently by direct interpolation. The aft-radiation version of this code models the shear layer emanating from the shroud for including its refraction effects on sound propagation based on some kinematic approximations. While frequency-domain methods are not as efficient as the time-domain methods for broadband noise predictions, and are cumbersome to use for multifrequency noise sources, they provide important insight into the functioning of liner materials that are generally

tuned to resonate at a single frequency or a narrow band of discrete frequencies. Furthermore, the use of frequency-domain methods eliminates questions regarding the accurate resolution of temporal characteristics associated with the prediction algorithm.

The goal of this paper is to describe a recently developed, parallel, frequency-domain code that includes the effects of non-uniform background flows and acoustic treatment. This code resorts only to the linearization of the Euler equations about a mean flow that comes from CFD solutions, so that its refraction effects on sound propagation are included in computations more realistically. This would be particularly important for high-speed flows through inlets and also for aft radiation from turbofans where the shear layer emanating from the shroud of the engine may cause significant refraction of the emitted sound waves. Although it is easily extendable to aft radiation, the present approach has been applied only to fore-radiation problems in the paper.

The method is described in the next section. Then forward-radiation simulations are performed, including effects of liners, for a JT15D engine test inlet and a generic inlet. The JT15D results are compared with experimental data. It is demonstrated that the developed code is capable of making accurate forward-radiation predictions.

2. Mathematical model

2.1. Governing equations

The 3-D, time-dependent, linearized Euler equations are transformed into the frequency domain assuming perturbations of the primitive-dependent variables are of the form

$$\mathbf{Q}'(\mathbf{x},t) = \mathrm{Re}\{\hat{\mathbf{Q}}(x,r,\omega)\,\mathrm{e}^{\mathrm{i}\omega t+\mathrm{i}m\theta}\}, \tag{1}$$

where

$$\begin{aligned}\mathbf{Q}' &= [u',v',w',p']^{\mathrm{T}},\\ \hat{\mathbf{Q}} &= [\hat{u},\hat{v},\hat{w},\hat{p}]^{\mathrm{T}},\end{aligned} \tag{2}$$

and $\mathrm{i}=\sqrt{-1}$; u',v',w' are the velocity perturbations in the cylindrical x,r,θ co-ordinate directions, respectively; p is the pressure; and a hat on a variable indicates a complex quantity. In Eq. (1), ω is the circular frequency and the integer m represents the azimuthal mode number.

Upon substitution of Eq. (1) into the Euler equations linearized about a non-uniform, axisymmetric flow, in cylindrical co-ordinates the equations governing the complex amplitudes of the flow perturbations become

$$\mathrm{i}\omega\hat{u}+u_0\frac{\partial\hat{u}}{\partial x}+v_0\frac{\partial\hat{u}}{\partial r}+\hat{u}\frac{\partial u_0}{\partial x}+\hat{v}\frac{\partial u_0}{\partial r}+\frac{1}{\rho_0}\frac{\partial\hat{p}}{\partial x}-\frac{\hat{p}}{\rho_0^2c_0^2}\frac{\partial p_0}{\partial x}=0, \tag{3}$$

$$\mathrm{i}\omega\hat{v}+u_0\frac{\partial\hat{v}}{\partial x}+v_0\frac{\partial\hat{v}}{\partial r}+\hat{u}\frac{\partial v_0}{\partial x}+\hat{v}\frac{\partial v_0}{\partial r}+\frac{1}{\rho_0}\frac{\partial\hat{p}}{\partial r}-\frac{\hat{p}}{\rho_0^2c_0^2}\frac{\partial p_0}{\partial r}=0, \tag{4}$$

$$\mathrm{i}\omega\hat{w}+u_0\frac{\partial\hat{w}}{\partial x}+v_0\frac{\partial\hat{w}}{\partial r}+\frac{\mathrm{i}m}{\rho_0 r}\hat{p}+\frac{v_0\hat{w}}{r}=0, \tag{5}$$

$$\mathrm{i}\omega\hat{p} + u_0\frac{\partial\hat{p}}{\partial x} + v_0\frac{\partial\hat{p}}{\partial r} + \hat{u}\frac{\partial p_0}{\partial x} + \hat{v}\frac{\partial p_0}{\partial r} + \gamma p_0\left(\frac{\partial\hat{u}}{\partial x} + \frac{\partial\hat{v}}{\partial r} + \frac{\hat{v}}{r} + \frac{\mathrm{i}m}{r}\hat{w}\right) + \gamma\hat{p}\left(\frac{\partial u_0}{\partial x} + \frac{\partial v_0}{\partial r} + \frac{v_0}{r}\right) = 0, \tag{6}$$

where $[\rho_0, u_0, v_0, p_0]^{\mathrm{T}}$ represent the non-uniform, axisymmetric, mean flow states. Note that the above equations contain derivatives only in 2-D (x, r) and the periodic, azimuthal variations have been transformed only to source-like terms multiplied by im. Hence, the 3-D field of a single spinning mode needs to be solved only in the (x, r) co-ordinates, reducing the computational expense of full 3-D simulations greatly.

Eqs. (3)–(6) are transformed into a body-fitted curvilinear co-ordinate system through the mappings

$$x = x(\xi, \eta); \quad r = r(\xi, \eta), \tag{7}$$

where (x, r) are the axial and radial co-ordinates, and (ξ, η) are the curvilinear co-ordinates.

2.2. Boundary conditions

2.2.1. Fan-face conditions

Exact cylindrical duct eigensolutions are used at the fan face to excite the acoustic field, which is assumed to be a deviation from the mean field. Acoustic pressure amplitude at a constant x plane in a circular annular duct is given by

$$\hat{p}(r, \theta) = \sum_{m,\mu} A_{m\mu}\left[\mathrm{J}_m(k_{m\mu}r) + Q_{m\mu}\mathrm{Y}_m(k_{m\mu}r)\right]\mathrm{e}^{\mathrm{i}(m\theta)}, \tag{8}$$

where m and μ are the azimuthal and radial mode orders, respectively; $A_{m\mu}$ is the amplitude of the (m, μ) mode; J_m and Y_m are the mth order Bessel functions of the first and second kinds, respectively; $k_{m\mu}$ are the eigenvalues that make the transcendental equation zero resulting from the wall condition, $\partial\hat{p}/\partial r|_{wall} = 0$; $Q_{m\mu} = -\mathrm{J}'_m(\sigma k_{m\mu})/\mathrm{Y}'_m(\sigma k_{m\mu})$ in which a prime indicates a derivative with respect to r, and σ is the hub-to-tip ratio. When there is no centerbody (i.e., $\sigma = 0$), $Q_{m\mu}$ is zero. The azimuthal mode order m is found using the rotor–stator interaction theory of Tyler and Sofrin [15]. According to this theory, the circumferential mode order m is given by $m = nB + sV$, where B and V are the numbers of rotor blades and stator vanes, respectively, n is the time harmonic index and s is any integer number. The number of rotor blades, number of exit guide vanes and the rotor speed are entered as part of the input to the code, and the modes that are cut on are automatically determined based on the local mean flow conditions at the source plane, which is usually taken as the fan face. Outflow boundary conditions are applied at the source plane in conjunction with Eq. (8). The non-reflecting conditions of Giles [16,17] are adapted to the present work to introduce the incident acoustic waves into the domain while letting the outgoing ones leave it with minimal reflection. The adapted conditions are given in the frequency domain by

$$\mathrm{i}\omega\hat{u} + \frac{(u_0 + c_0)}{2\rho_0 c_0}\left(\frac{\partial\hat{p}}{\partial x} + \rho_0 c_0\frac{\partial\hat{u}}{\partial x}\right) + \frac{(c_0 - u_0)}{4}\left(\frac{\partial\hat{v}}{\partial r} + \frac{\hat{v}}{r} + \frac{\mathrm{i}m}{r}\hat{w}\right) = \mathrm{i}\omega\hat{\mathscr{L}}_1/\rho_0 c_0, \tag{9}$$

$$\mathrm{i}\omega\hat{v} + u_0\frac{\partial\hat{v}}{\partial x} + \frac{1}{\rho_0}\frac{\partial\hat{p}}{\partial r} = 0, \tag{10}$$

$$\mathrm{i}\omega\hat{w} + u_0\frac{\partial\hat{w}}{\partial x} + \frac{\mathrm{i}m}{\rho_0 r}\hat{p} = 0, \tag{11}$$

$$\mathrm{i}\omega\hat{p} + \frac{u_0 + c_0}{2}\left(\frac{\partial\hat{p}}{\partial x} + \rho_0 c_0\frac{\partial\hat{u}}{\partial x}\right) + \frac{(3c_0 + u_0)}{4}\rho_0 c_0\left(\frac{\partial\hat{v}}{\partial r} + \frac{\hat{v}}{r} + \frac{\mathrm{i}m}{r}\hat{w}\right) = -\mathrm{i}\omega\hat{\mathscr{L}}_1, \tag{12}$$

where $\hat{\mathscr{L}}_1$ is set equal to the incident (upstream travelling) part of the acoustic pressure given by Eq. (8). Numerical experimentation has shown that these conditions do not completely eliminate the outgoing waves. Even for some cases, specifying acoustic pressure directly from Eq. (8) and solving the other perturbed quantities from the interior equations yielded better results.

2.2.2. Hard-wall conditions

Consistent with the Euler equations fluid particles are let slip at a hard wall under the influence of pressure fluctuations. Numerically, the normal component of the contravariant velocity perturbation is set to zero. That is, on an orthogonal mesh at the wall,

$$\hat{V}_C = \eta_x\hat{u} + \eta_r\hat{v} = 0. \tag{13}$$

The value of the tangential contravariant velocity perturbation $\hat{U}_C = \xi_x\hat{u} + \xi_r\hat{v}$ is extrapolated from the interior solution. The azimuthal velocity $\hat{w}$ is also extrapolated from the interior solution. The pressure perturbation is then found from the normal momentum balance given, assuming the grid lines are orthogonal at the wall, as

$$\partial\hat{p}/\partial\eta = -[2\rho_0 v_{0,t}\hat{v}_t + (\hat{p}/c_0^2)v_{0,t}^2][\eta_x^2 + \eta_r^2]^{-1/2}\,R^{-1}, \tag{14}$$

where $v_{0,t}$ and $\hat{v}_t$ are the mean tangential velocity and tangential velocity perturbation, respectively, c_0 is the local speed of sound ($c_0^2 = \gamma p_0/\rho_0$), and R is the radius of wall curvature, which may be found using the transformation metrics at the wall.

2.2.3. Impedance condition

Acoustic impedance condition is applied on acoustically treated surfaces (liner). Because fluid particles are allowed to slip at a wall and because a non-zero normal velocity exists on an acoustic treatment panel, the same momentum equations as the interior are solved, but the energy equation is replaced with the impedance condition equation, given as [18]

$$\mathrm{i}\omega\hat{p} + \mathscr{L}_0\hat{p} = -\mathrm{i}\omega\,Z(\omega)\,\hat{v}_n, \tag{15}$$

where $\hat{v}_n$ is the normal component of the velocity perturbation, and $Z(\omega)$ is the frequency-dependent impedance. The spatial operator $\mathscr{L}_0$ of Eq. (15) is given in the curvilinear co-ordinates by

$$\mathscr{L}_0 = U_{0,C}\partial/\partial\xi + \boldsymbol{\nabla}\eta\cdot\partial\mathbf{V}_0/\partial\eta, \tag{16}$$

where ξ is the grid line along the surface, $U_{0,C}$ is the mean tangential contravariant velocity and $\mathbf{V}_0$ is the mean velocity. The last term of the $\mathscr{L}_0$ operator is neglected in the present paper since its

value is usually small on low curvature surfaces. An alternate form of the impedance condition was proposed by Eversman [19] retaining the mean velocity gradient related term. Although it was not adopted in the present work, this form could be easier to use in numerical algorithms of the present type.

The equation governing the normal velocity perturbation can be written at the wall as

$$\mathrm{i}\omega\hat{v}_n + U_{0,C}\frac{\partial\hat{v}_n}{\partial\xi} + |\nabla\eta|\left[\frac{v_{0,n}}{\partial\eta}\hat{v}_n + \frac{1}{\rho_0}\frac{\partial\hat{p}}{\partial\eta} - \frac{\hat{p}}{\rho_0^2 c_0^2}\frac{\partial p_0}{\partial\eta}\right] + \frac{2v_{0,t}\hat{v}_t}{R} = 0, \tag{17}$$

where $v_{0,n}$ and $v_{0,t}$ are the mean normal and tangential velocities, respectively, and $\hat{v}_t$ is the tangential velocity perturbation. Upon substitution of the normal velocity perturbation from Eq. (17) into Eq. (15), an equation governing the pressure perturbation along a lined surface is obtained in the following form:

$$A\frac{\partial^2\hat{p}}{\partial\xi^2} + B\frac{\partial\hat{p}}{\partial\xi} + C\frac{\partial\hat{p}}{\partial\eta} + D\hat{p} + E = 0, \tag{18}$$

where

$$A = \frac{U_{0,C}^2}{\mathrm{i}\omega Z}, \tag{19}$$

$$B = \frac{U_{0,C}}{\mathrm{i}\omega Z}\left[2\mathrm{i}\omega + \frac{\partial U_{0,C}}{\partial\xi} + |\nabla\eta|\frac{\partial v_{0,n}}{\partial\eta}\right], \tag{20}$$

$$C = -|\nabla\eta|/\rho_0, \tag{21}$$

$$D = \frac{\mathrm{i}\omega}{Z} + \frac{|\nabla\eta|}{Z}\frac{\partial v_{0,n}}{\partial\eta} + \frac{|\nabla\eta|}{\rho_0^2 c_0^2}\frac{\partial p_0}{\partial\eta}, \tag{22}$$

$$E = -2v_{0,t}\hat{v}_t/R. \tag{23}$$

Eq. (18) is solved on a soft wall after the interior and hard-wall solutions are updated explicitly at every stage of the Runge–Kutta (R–K) algorithm that will be described later. Eq. (18) is discretized implicitly in pressure, which results in a linear system of equations. The tangential velocity perturbations required by these equations (through the E term) are extrapolated from the available interior solution. In this implicit approach, the pressure amplitudes needed from the interior grid points are set equal to the available values of those obtained explicitly from the R–K stage.

2.2.4. Farfield boundary conditions

Non-reflecting boundary conditions are solved on the outer, farfield boundaries. The first order spherical damper condition operator of Bayliss and Turkel [20] is used on the inflow parts of these boundaries. This is similar to that proposed by Tam and Webb [21]. On the outflow parts, the linearized momentum equations are solved for the velocity perturbations, but the radiation operator is applied to the pressure perturbation as suggested by Tam and Webb [21]. All farfield boundary conditions are also transformed to the frequency domain and recast in cylindrical co-ordinates so that the same mapping transformations as the interior apply to them.

2.3. Discretizations

A direct discretization of the governing equations and the farfield boundary conditions would result in a large linear system of equations in the complex unknowns $\hat{u}$, $\hat{v}$, $\hat{w}$, and $\hat{p}$. Solution of such equation systems is not usually efficient in distributed computing environments. The suitability of the explicit algorithms to parallel computing can, however, be exploited for solution of the present frequency-domain equations by introducing a pseudo-time derivative to and discretizing them explicitly. This approach allows use of well-known explicit time integration methods and well-known convergence acceleration techniques (not done in this study) for rapid solutions of the equations of this type.

The interior and the farfield boundary equations are written in the form

$$\frac{\mathrm{d}\hat{\mathbf{Q}}}{\mathrm{d}\tau} + \hat{\mathbf{R}}(\hat{\mathbf{Q}}) = 0, \tag{24}$$

where $\hat{\mathbf{R}}(\hat{\mathbf{Q}})$ represents the semi-discretized governing equations and the farfield boundary conditions in curvilinear co-ordinates, and $\mathrm{d}\hat{\mathbf{Q}}/\mathrm{d}\tau$ is the pseudo-time derivative term added to the equations. A four-stage R–K time integration scheme is employed to drive the solution to a steady harmonic state iteratively. Spatial derivatives are evaluated using fourth order accurate finite differences in general but in the developed code second order accurate differences are also available as an option. It should be noted that in the present approach the dependent quantities are the amplitudes of the perturbations which will exhibit small spatial variations in cases of weak wave reinforcements or cancellations, or decay. In such cases, the present approach requires usually a coarser mesh or spatially lower order discretization than a time-domain approach in which the peaks and valleys of a wave must be properly resolved for accurate computation. Nevertheless, fourth order differences were used for all the computations of the present study. The R–K scheme is given by

$$\begin{aligned}
\hat{\mathbf{Q}}^{(0)} &= \hat{\mathbf{Q}}^{n}, \\
\hat{\mathbf{Q}}^{(1)} &= \hat{\mathbf{Q}}^{n} - \tfrac{1}{4}\Delta\tau[\hat{\mathbf{R}}(\hat{\mathbf{Q}}^{(0)}) - \hat{\mathbf{D}}(\hat{\mathbf{Q}}^{(0)})], \\
\hat{\mathbf{Q}}^{(2)} &= \hat{\mathbf{Q}}^{n} - \tfrac{1}{3}\Delta\tau[\hat{\mathbf{R}}(\hat{\mathbf{Q}}^{(1)}) - \hat{\mathbf{D}}(\hat{\mathbf{Q}}^{(0)})], \\
\hat{\mathbf{Q}}^{(3)} &= \hat{\mathbf{Q}}^{n} - \tfrac{1}{2}\Delta\tau[\hat{\mathbf{R}}(\hat{\mathbf{Q}}^{(2)}) - \hat{\mathbf{D}}(\hat{\mathbf{Q}}^{(0)})], \\
\hat{\mathbf{Q}}^{n+1} &= \hat{\mathbf{Q}}^{n} - \Delta\tau[\hat{\mathbf{R}}(\hat{\mathbf{Q}}^{(3)}) - \hat{\mathbf{D}}(\hat{\mathbf{Q}}^{(0)})],
\end{aligned} \tag{25}$$

where superscript n shows the iteration step, $\Delta\tau$ is the pseudo-time step size from an iteration step to the next, and $\hat{\mathbf{D}}(\hat{\mathbf{Q}})$ is artificial dissipation which is used to suppress the development of spurious waves. A fourth order, constant coefficient dissipation model was employed in all the computations presented in the paper.

In the present work, the grid is generated such that, on the mapped computational domain, the walls and the centerline of the engine are located midway between two grid points: one ghost point in the wall and the first interior point off the wall. Therefore, when the wall conditions are applied interpolation of data to the wall is required. Third order interpolation is used for a globally fourth order accurate scheme.

2.4. Farfield predictions

Farfield sound is computed using a modified version of the Kirchhoff method that was previously developed by the authors [2]. In this method, the Kirchhoff formula given by Farassat and Myers [22] is integrated using a forward time binning approach. When the solution is converged, a 3-D Kirchhoff surface is constructed by revolving a curve (a grid line or a set of grid lines) from the 2-D grid 360° around the engine axis, and the computed acoustic data on this curve are discretely distributed over the constructed Kirchhoff surface for one wave period according to Eq. (1). Then the discrete data on the Kirchhoff surface are integrated for specified farfield observer locations using the aforementioned Kirchhoff method. When the present code is extended to aft radiation including the effects of shear layers on the radiation sound field, the Ffowcs Williams–Hawkings (FW–H) equation based farfield prediction method of Long et al. [23] could be more appropriate.

2.5. Parallel computing

Distributed computing approach is used in the present study. In this approach, the computational grid is divided into smaller domains and each subdomain is assigned to a different processor that is on a network. The necessary data exchange across a shared boundary between two neighboring subdomains is realized via library routines from the message passing interface (MPI) standard.

3. Results and discussion

3.1. Radiation of $(13,0)$ mode from JT15D inlet

The present method is verified first considering radiation from the small JT15D turbo-fan inlet which has been studied both computationally [10,2] and experimentally [24,25]. A modified, static test version of the inlet is adopted for the present study since experimental data are available for it with liners [24,25]. The test engine has a uniform inlet cross-section and a round nacelle lip, as shown in Fig. 1. The engine has a fan with a diameter of 53.5 cm and hub-to-tip ratio of approximately 0.37. In the experiments reported in Refs. [24,25], a spinning $(13,0)$ mode was generated in a controlled manner with a 28-bladed rotor interacting with 41 rods installed just ahead of the fan. The tested engine speed corresponded to a blade passing frequency (BPF) of 3150 Hz. In the present computations, the mass flow through the inlet is set to 11.62 kg/s, to yield a mean Mach number of about 0.147 at the fan stage matching that of the experiments. Based on these local conditions, the cut-off ratio for the $(13,0)$ mode is calculated as 1.05, and the corresponding dimensionless frequency parameter $(\omega r/c_0)_f = (kr)_f$ is 15.5. The lining material is chosen to have a length of 8 cm and located in the inlet such that the liner trailing edge is about 12 cm ahead of the fan face. A mesh with 241×81 grid points is used for the computations. The grid points are distributed nearly evenly in the direction of propagation with about 15 points per wavelength. This resolution will be sufficient to capture the amplitude and phase variations of the waves of interest. The mesh is shown in Fig. 1, where also illustrated are the two different

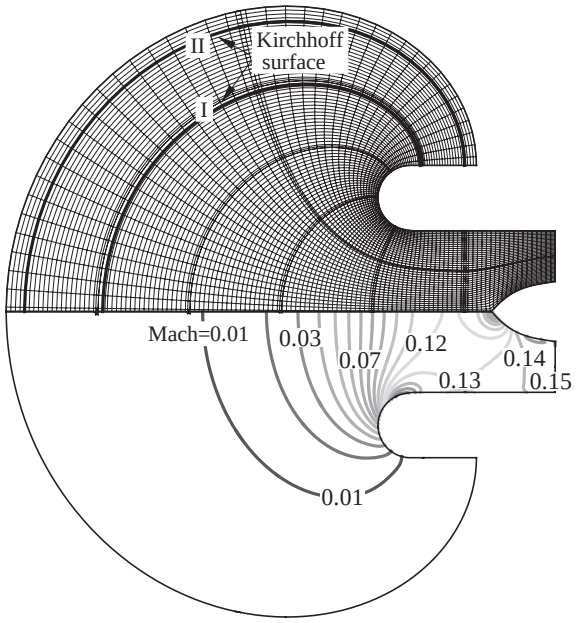

Fig. 1. Static test JT15D mesh (241 × 81 points, every other grid line is shown) and mean Mach number contours. $M_\infty = 0,\ \dot{m} = 11.62$ kg/s.

Kirchhoff surfaces used for farfield predictions. The mesh is divided into 12 subdomains for parallel computing. Fig. 1 also shows in the lower half the computed mean Mach number contours. The mean flow was calculated with a residual reduction of about eight orders of magnitude using a separate, fourth order accurate, full Euler solver [2]. It is clear from the figure that the flow is entrained into the engine under the influence of a favorable pressure gradient created at the fan through boundary conditions, although the engine is at a static condition. The flow accelerates from outside of the nacelle into the engine reaching the highest values just inside the nacelle lip and near the fan. An average Mach number of nearly 0.147 was captured at the fan. Although from the Mach number contours it is clear that the flow is not exactly uniform at the fan stage, the deviations in the mean flow quantities from their uniform counterparts were determined to be within only 2–3 per cent, and this created no problem for the acoustic computations using the fan-face conditions discussed earlier.

It was indicated above that the (241 × 81)-point mesh would have enough resolution to capture the waves of interest. Nevertheless its sufficiency is demonstrated here, obtaining the hard-wall solution also on a 1.5 times finer grid in each direction (i.e., on a (361 × 121)-point grid) and comparing the results of both meshes. This comparison is made for the contours of acoustic pressure amplitudes in Fig. 2. It is clear that the acoustic fields of both grids are almost identical, indicating the grid independency of the solutions on the (241 × 81)-point mesh. Hence, this mesh was used for all the acoustic computations presented below.

Along with the hard-wall case, two soft-wall cases with specific impedances of $Z_{sp} = Z/\rho_\infty c_\infty = 0.638 + 0.5\mathrm{i}$ and $1.136 + 0.5\mathrm{i}$, respectively, were also run at the aforementioned operating conditions. Fig. 3 shows the computed sound pressure level (SPL) contours for the hard- and the soft-wall case with $Z_{sp} = 0.638 + 0.5\mathrm{i}$. The radiation directions for both cases are

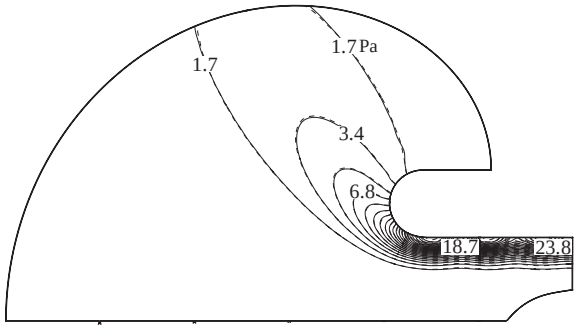

Fig. 2. Comparison of contours of acoustic pressure amplitudes computed on the (241 × 81) and (361 × 121)-point meshes, $M_\infty = 0$, $\dot{m} = 11.62$ kg/s. ——, (241 × 81)-point grid; - - - - , (361 × 121)-point grid.

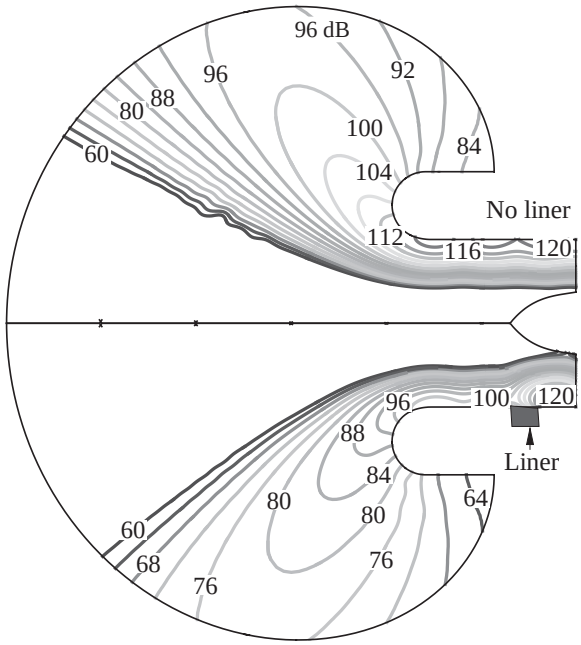

Fig. 3. SPL contours (dB): Upper half with a hard wall, lower half with a liner having $Z_{sp} = 0.638 + 0.5$i. Source (13, 0) mode at $BPF = 3150$ Hz, $M_\infty = 0$, $\dot{m} = 11.62$ kg/s, $(kr)_f = 15.5$.

evident. Sound attenuation effects of the liner material are clearly seen from comparison of the plotted SPL contours.

Effects of the Kirchhoff surface location on the farfield predictions are assessed before presenting and comparing the hard- and lined-wall farfield predictions. The hard-wall farfield solutions from the two Kirchhoff surfaces, which were shown in Fig. 1, are plotted together with experimental data [24,25] in Fig. 4. Excellent agreement between the predictions of the two Kirchhoff surfaces is evident. This indicates that both Kirchhoff surfaces were adequate for farfield calculations, and the increased mesh spacing in the tangential direction to the surfaces was

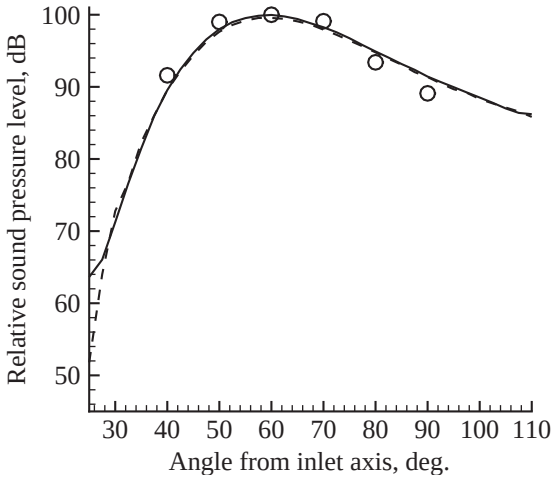

Fig. 4. Effect of Kirchhoff surface location on farfield SPL of the hard-walled inlet. Source (13, 0) mode at $BPF = 3150$ Hz, $M_\infty = 0$, $\dot{m} = 11.62$ kg/s, $(kr)_f = 15.5$. ——, Kirchhoff surface I; - - - -, Kirchhoff surface II; ○ ○ ○, experimental data.

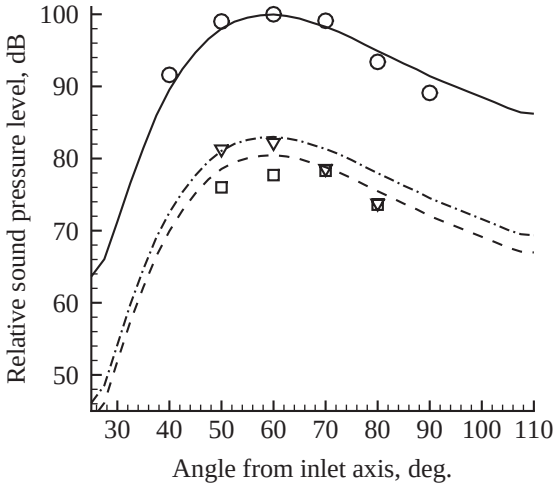

Fig. 5. Farfield SPLs of the JT15D inlet: Source (13, 0) mode at $BPF = 3150$ Hz, $M_\infty = 0$, $\dot{m} = 11.8$ kg/s, $(kr)_f = 15.5$. Present computations: ——, hard wall; - - - -, lined wall, $Z_{sp} = 0.638 + 0.5$i; — · —, lined wall, $Z_{sp} = 1.136 + 0.5$i; and experimental data: ○, hard wall; □, lined wall, $Z_{sp} = 0.638 + 0.5$i; ▽, lined wall, $Z_{sp} = 1.136 + 0.5$i.

unimportant. Therefore, in comparison of the lined-wall computations with experimental data, Kirchhoff surface location I was used.

The predicted farfield results are shown in Fig. 5 for the hard- and lined-wall cases along with the experimental data [24,25]. All the computed results were normalized such that the hard-wall SPL at 60° from the engine axis was 100 dB. The same normalization was also applied to the experimental data. This was necessary since no exact acoustic source strength information was available to simulate the actual conditions. It is clear from the figure that the hard-wall solution

agrees quite well with the experimental data. The soft-wall calculations and the corresponding experimental data also agree well on the general attenuation rates of about 20 dB. However, this agreement is better at higher angles for $Z_{sp} = 0.638 + 0.5\mathrm{i}$, while this is true at lower angles for $Z_{sp} = 1.136 + 0.5\mathrm{i}$. It is interesting that the predicted attenuation rates are almost constant at all angles, and there is about 2–3 dB difference between the attenuation rates of both liners. However, the measured attenuation rates for the two liners indicate about a 5 dB difference at 50° and 60°, and almost no difference at 70° and 80°. Of course, when a liner is present, there are scattered waves from the liner leading and trailing edges. These scattered waves travel both downstream and upstream. Part of the downstream propagating waves might have been reflected back into the domain in the experiments. Because of lack of information on this, no such actual phenomenon could be simulated in the present work. Therefore, this may have played a role on the observed slight deviations of the computed results from the measured data.

3.2. *Radiation of* (6, 0) *and* (6, 1) *modes from a generic engine*

It is not only the liner impedance but also its installation location that plays an important role in attenuating the sound waves propagating through an engine inlet. This is illustrated in this section by predicting the sound fields of the spinning (6, 0) and (6, 1) modes from a generic engine inlet lined with two different liner impedances. Preserving the lengths of the liners, their installation positions are changed and the effects of this on the radiated acoustic fields are demonstrated. The liner specific impedances are chosen arbitrarily as $2.17 - 1.98\mathrm{i}$ and $4.01 - 1.01\mathrm{i}$. These values were actually given by a model impedance function of another code [26]. The inlet has a diameter of 55.9 cm at the fan stage and the hub-to-tip ratio is 0.35. The free-stream Mach number and the mass flow rate are taken as 0.2 and 17.8 kg/s, respectively. The engine has 18 fan rotor blades and 42 stator vanes. When the fan rotor has a speed of 5200 r.p.m., the spinning (6, 0) and (6, 1) modes are cut on at $2BPF$, 3120 Hz. At the indicated operating conditions, the corresponding dimensionless frequency parameter $(kr)_f$ is found as 16.1. First, a combination of the (6, 0) and (6, 1) modes is investigated. Then the (6, 0) mode is evaluated alone.

3.2.1. (6, 0) + (6, 1) *Modes*

The (6, 0) and (6, 1) modes are combined with a 45° phase difference, and their modal amplitudes are set equal. Since the dimensionless frequency of these modes is close to that of the (13, 0) mode studied in Section 3.1, a (241×81)-point grid must be capable of resolving the (6, 0) and (6, 1) modes properly. The generated mesh is shown in Fig. 6. The required mean flow was calculated using again a fourth order accurate Euler solver. The computed mean Mach number contours are shown also in Fig. 6. Variations in the background flow are evident. It is certain that such variations would be much stronger and consequently more influential on acoustic propagation at high Mach numbers.

Fig. 7 shows the acoustic pressure amplitudes for the hard-walled inlet (upper half of the figure) and lined inlet (lower half) with $Z_{sp} = 2.17 - 1.98\mathrm{i}$ and position I, which signifies a close placement of the liner to the fan. Liner position II denotes a far upstream placement. It is clear from Fig. 7 that there is basically a single but wide dominating lobe radiated from the hard-walled inlet, while two equally important lobes appear when the inlet walls are lined. In the latter case the inner lobe (that radiating in a direction closer to the inlet axis) is narrower than the outer lobe.

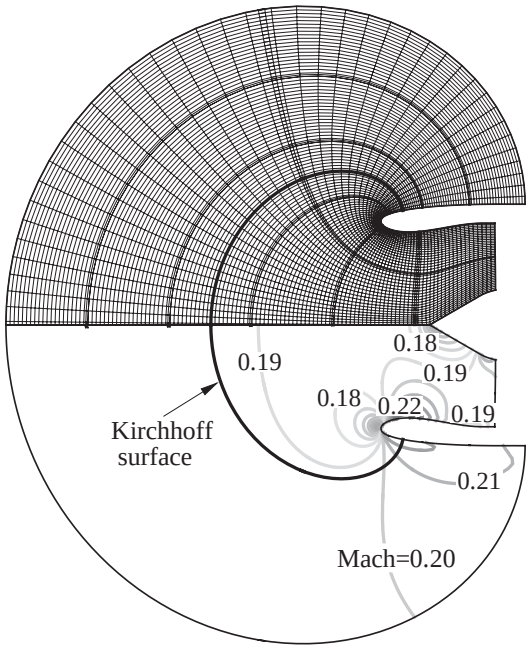

Fig. 6. Generic engine mesh (241×81 points, every other grid line is shown) and the mean Mach number contours. $M_\infty = 0.2$, $\dot{m} = 17.8$ kg/s.

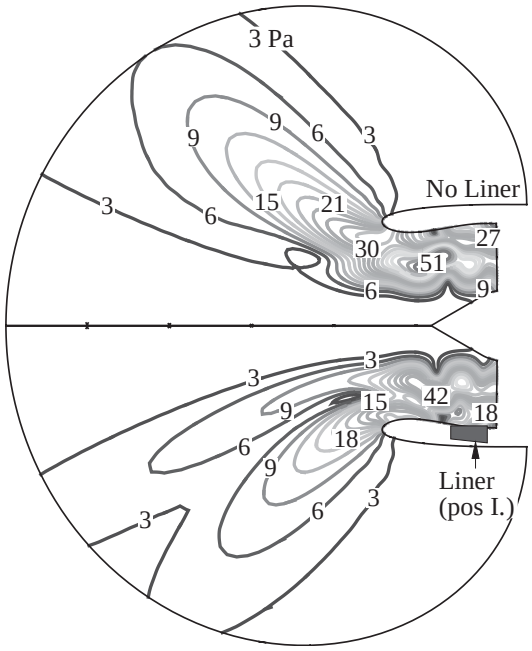

Fig. 7. Contours of acoustic pressure amplitude for the generic inlet: Upper half without liner, lower half with liner having $Z_{sp} = 2.17 - 1.98$i. Source $(6,0) + (6,1)$ modes with 45° phase difference, $2BPF = 3120$ Hz, $M_\infty = 0.2$, $\dot{m} = 17.8$ kg/s, $(kr)_f = 16.1$.

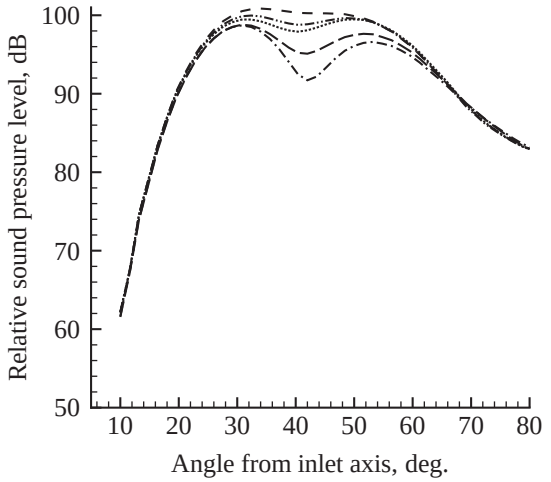

Fig. 8. Farfield SPLs of the generic engine: Source $(6,0)+(6,1)$ modes with 45° phase difference, $2BPF = 3120$ Hz, $M_\infty = 0.2$, $\dot{m} = 17.8$ kg/s, $(kr)_f = 16.1$. - - - -, hard wall; – · –, liner position I, $Z_{sp} = 2.17 - 1.98$i; ⋯⋯, liner position II, $Z_{sp} = 2.17 - 1.98$i; — —, liner position I, $Z_{sp} = 4.01 - 1.01$i; – · · –, liner position II, $Z_{sp} = 4.01 - 1.01$i.

These are all clear also from the farfield directivities presented for the hard- and all-lined-wall cases in Fig. 8. It is indicated that when the liner with $Z_{sp} = 2.17 - 1.98$i is placed away from the fan (position II), its attenuation effect appears to decrease significantly in a direction about 42° from the inlet axis. An approximately 8 dB difference is observed in this direction between the two liner locations. Similar trends are observed for $Z_{sp} = 4.01 - 1.01$i, but with less change in attenuation due to the position change. When the attenuation rates yielded by both impedance values are compared, $Z_{sp} = 2.17 - 1.98$i seems more effective.

3.2.2. $(6,0)$ *Mode*

The $(6,0)$ mode was also run alone in order to understand which mode was actually attenuated more in the results of the previous section. The same liner impedances and positions were considered. The resultant acoustic pressure fields are shown in Fig. 9 for the hard-walled inlet and lined inlet with liner position I and $Z_{sp} = 2.17 - 1.98$i. It is clear that the sound field of the $(6,0)$ mode for the hard-wall case has a narrower main lobe than that resulted from the combination of the $(6,0)$ and $(6,1)$ modes. This indicates that the $(6,1)$ mode had a significant contribution to the wider lobe resulting from the two modes, and the $(6,1)$ mode radiates actually at a higher angle from the axis. This can also be observed when the farfield SPL plots given in Figs. 8 and 10 are compared. It is interestingly evident from the SPL plots of the $(6,0)$ mode alone (Fig. 10) that, while a liner causes some attenuation for the main lobe, part of the acoustic energy is redirected to higher angles causing a higher SPL side lobe. Also when closely examined, liner position II appears to yield more attenuation than position I as opposed to the preceding case. This means that liner position I is more efficient for attenuating the $(6,1)$ mode than the $(6,0)$ mode. When the attenuation rates yielded by both liners are compared, again $Z_{sp} = 2.17 - 1.98$i is found to be more effective.

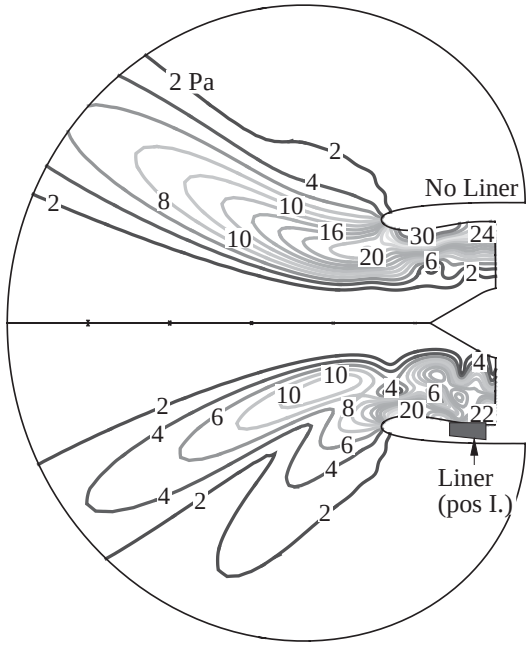

Fig. 9. Contours of acoustic pressure amplitude for the generic inlet: Upper half without liner, lower half with liner having $Z_{sp} = 2.17 - 1.98\text{i}$. Source (6, 0) mode only, $2BPF = 3120$ Hz, $M_\infty = 0.2$, $\dot{m} = 17.8$ kg/s, $(kr)_f = 16.1$.

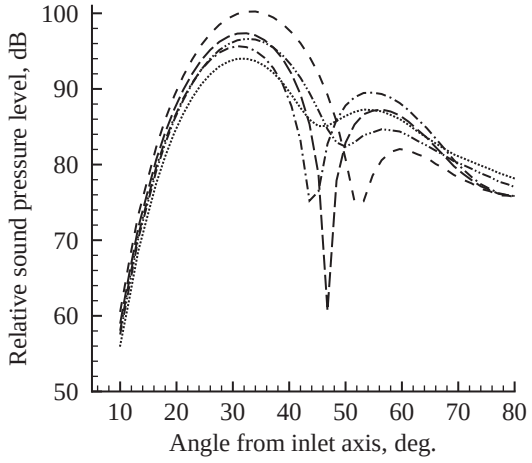

Fig. 10. Farfield SPLs of the generic engine: Source (6, 0) mode only, $2BPF = 3120$ Hz, $M_\infty = 0.2$, $\dot{m} = 17.8$ kg/s, $(kr)_f = 16.1$. - - - -, hard wall; – · –, liner position I, $Z_{sp} = 2.17 - 1.98\text{i}$; · · · ·, liner position II, $Z_{sp} = 2.17 - 1.98\text{i}$; — —, liner position I, $Z_{sp} = 4.01 - 1.01\text{i}$ – · · –, liner position II, $Z_{sp} = 4.01 - 1.01\text{i}$.

4. Convergence and computational performance

The runs presented in this paper required 40 000–60 000 steps for an acoustic field to converge. For convergence, the L_2 norm of $\partial\hat{p}/\partial\tau$ was monitored, especially in the outer computational domain near the Kirchhoff surface. An example residual history is shown in Fig. 11. This figure

shows the residual variation with the iteration count for the (6, 0) mode radiating from the generic engine with $Z_{sp} = 2.17 - 1.98i$. Since the source is introduced at the fan face, the residual is zero in early iterations, but later acoustic perturbations are felt in the outer domain giving rise to increased values and a peak of the residual. As the solution is advanced through the R–K iterations, a clear residual reduction is observed. Although the rate at which this residual reduction is not great, no significant variations are observed in the acoustic field from one iteration to another after about two orders of magnitude residual reduction from the peak. The solution at this point is assumed to have converged. This situation is illustrated in Fig. 12. In this figure, the acoustic fields at two different iteration levels are compared. The solid contour lines indicate the results at the 26 000th iteration and the dashed lines indicate the results at the 30 000th iteration. Even at these iteration levels both fields look nearly identical. Of course the convergence may be accelerated using one of the standard convergence acceleration techniques, such as the multigrid method, but none of them has been implemented in this work.

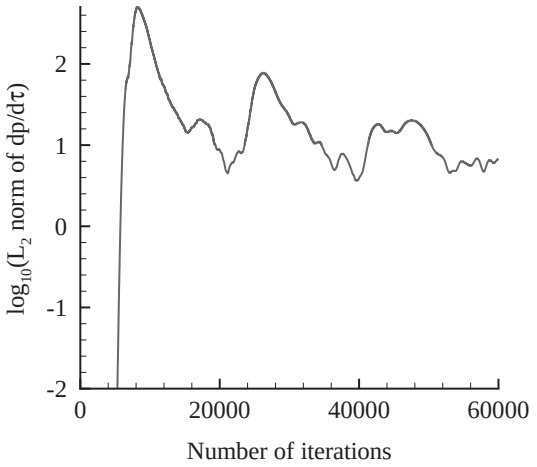

Fig. 11. Convergence history: Source (6, 0) mode only, $2BPF = 3120$ Hz, $M_\infty = 0.2$, $\dot{m} = 17.8$ kg/s, $(kr)_f = 16.1$, $Z_{sp} = 2.17 - 1.98i$.

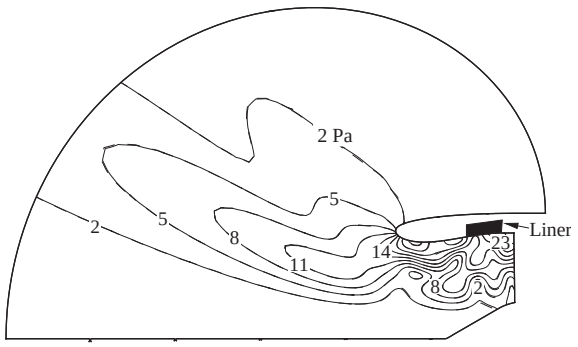

Fig. 12. Sound fields at two different solution steps: Source (6, 0) mode only, $2BPF = 3120$ Hz, $M_\infty = 0.2$, $\dot{m} = 17.8$ kg/s, $(kr)_f = 16.1$, $Z_{sp} = 2.17 - 1.98i$. ——, 26 000 iterations; - - - -, 30 000 iterations.

The developed code was run on a cluster of Pentium III, 700 MHz processors. A total of 12 processors were used for all the cases. The CPU time required for the computations was 1.61 s per grid point per R–K iteration on one processor. Thus, a converged solution on a 241×81 grid through 40 000–60 000 steps required about 2.9–4.3 h on 12 processors. A study on parallelization efficiency showed that the code scales reasonably well up to 16 processors. Hence, the computation times could be further reduced by using more processors.

5. Conclusions

A frequency-domain method has been developed for predicting sound fields of ducted fans. The method is based on the solution of the frequency-domain form of the Euler equations linearized about an axisymmetric non-uniform background flow. Solutions are carried out employing an explicit pseudo-time marching technique, which allows efficient solutions of equations of this type on parallel computers. Although it has not been implemented, a well-known convergence acceleration technique may readily be incorporated into the present approach due to its explicit nature. Example solutions were carried out for the JT15D engine inlet and for a generic engine inlet at various conditions. It was demonstrated by comparing the simulations of the former geometry to the available experimental data that the developed method accurately predicts the forward arc farfield sound of turbofans, including the attenuation effects of liners.

References

[1] T.L. Parrott, M.G. Jones, Parallel-element liner impedances for improved absorption of broadband sound in ducts, *Noise Control Engineering Journal* 43 (6) (1995) 183–195.

[2] Y. Özyörük, L.N. Long, Computation of sound radiating from engine inlets, *American Institute of Aeronautics and Astronautics Journal* 34 (5) (1996) 894–901.

[3] P.L. Spence, Ducted fan noise prediction using wave envelope analysis and the Kirchhoff formula, American Institute of Aeronautics and Astronautics Paper 97-1651-CP, *Proceedings of the Third/CEAS Aeroacoustics Conference*, Atlanta, GA, USA, May 1997, pp. 539–549.

[4] C.L. Rumsey, R.T. Biedron, F. Farassat, P.L. Spence, Ducted-fan engine acoustic predictions using a Navier–Stokes code, *Journal of Sound and Vibration* 213 (4) (1998) 643–664.

[5] I.B. Shim, J.W. Kim, D.J. Lee, Numerical study on radiation of multiple pure tone noise from an aircraft engine inlet, American Institute of Aeronautics and Astronautics Paper 99-1831, *Fifth American Institute of Aeronautics and Astronautics/CEAS Aeroacoustics Conference and Exhibit*, Bellevue, WA, USA, May 1999.

[6] D. Stanescu, D. Ait-Ali-Yahia, W.G. Habashi, M.P. Robichaud, Multidomain spectral computations of sound radiation from ducted fans, *American Institute of Aeronautics and Astronautics Journal* 37 (3) (1999) 296–302.

[7] V. Ahuja, Y. Özyörük, L.N. Long, Computational simulations of fore and aft radiation from ducted fans, American Institute of Aeronautics and Astronautics Paper 2000-1943, *Sixth American Institute of Aeronautics and Astronautics/CEAS Aeroacoustics Conference and Exhibit*, Hawaii, USA, June 2000.

[8] Y. Özyörük, L.N. Long, M.G. Jones, Time-domain numerical simulation of a flow-impedance tube, *Journal of Computational Physics* 146 (1) (1998) 29–57.

[9] R.J. Astley, W. Eversman, Wave envelope and finite element schemes for fan noise radiation from turbofan inlets, American Institute of Aeronautics and Astronautics Paper 83-0709, 1983.

[10] W. Eversman, A.V. Parrett, J.S. Preisser, R.J. Silcox, Contributions to the finite element solution of the fan noise radiation problem, *Transactions of the American Society of Mechanical Engineers* 107 (1985) 216–223.

[11] W. Eversman, I.D. Roy, Ducted fan acoustic radiation including the effects of nonuniform mean flow and acoustic treatment, American Institute of Aeronautics and Astronautics Paper 93-4424, 1993.
[12] W. Eversman, Aft fan duct acoustic radiation, CEAS/American Institute of Aeronautics and Astronautics Paper 95-155, June 1995.
[13] M. Nallasamy, D.L. Sutliff, L.J. Heidelberg, Propagation of spinning acoustic modes in turbofan exhaust ducts, *Journal of Propulsion and Power* 16 (5) (2000) 736–743.
[14] I.D. Roy, W. Eversman, Far-field calculations for turbofan noise, *American Institute of Aeronautics and Astronautics Journal* 39 (12) (2001) 2255–2261.
[15] J.M. Tyler, T.G. Sofrin, Axial flow compressor noise studies, *SAE Transactions* 70 (1962) 309–332.
[16] M.B. Giles, Nonreflecting boundary conditions for Euler equation calculations, *American Institute of Aeronautics and Astronautics Journal* 28 (12) (1990) 2050–2058.
[17] T. Colonius, S.K. Lele, P. Moin, Boundary conditions for direct computation of aerodynamic sound generation, *American Institute of Aeronautics and Astronautics Journal* 31 (9) (1993) 1574–1582.
[18] M.K. Myers, On the acoustic boundary condition in the presence of flow, *Journal of Sound and Vibration* 71 (3) (1980) 429–434.
[19] W. Eversman, The boundary condition at an impedance wall in a non-uniform duct with potential mean flow, *Journal of Sound and Vibration* 246 (1) (2001) 63–69.
[20] A. Bayliss, E. Turkel, Far field boundary conditions for compressible flow, *Journal of Computational Physics* 48 (1982) 182–199.
[21] C.K.W. Tam, J.C. Webb, Dispersion-relation-preserving finite difference schemes for computational acoustics, *Journal of Computational Physics* 107 (1993) 262–281.
[22] F. Farassat, M.K. Myers, Extension of Kirchhoff's formula for radiation from moving surfaces, *Journal of Sound and Vibration* 123 (1988) 451–460.
[23] L.N. Long, F. Souliez, A. Sharma, Aerodynamic noise prediction using parallel methods on unstructured grids, American Institute of Aeronautics and Astronautics Paper 2001-2196, *Seventh American Institute of Aeronautics and Astronautics/CEAS Aeroacoustics Conference*, Maastricht, The Netherlands, 28–30 May 2001.
[24] L.J. Heidelberg, E.J. Rice, L. Homyak, Acoustic performance of inlet suppressors on an engine generating a single mode, American Institute of Aeronautics and Astronautics Paper 81-1965, 1981.
[25] K.J. Baumeister, S.J. Horowitz, Finite element-integral acoustic simulation of JT15D turbofan engine, *Journal of Vibration, Acoustics, Stress, and Reliability in Design* 106 (1984) 405–413.
[26] Y. Özyörük, Parallel computation of forward radiated noise of ducted fans including acoustic treatment, *American Institute of Aeronautics and Astronautics Journal* 40 (3) (2002) 450–455.